Materials Horizons

ROYAL SOCIETY OF CHEMISTRY

COMMUNICATION

Cite this: *Mater. Horiz.*, 2020, 7, 2071

Received 5th March 2020, Accepted 12th May 2020

DOI: 10.1039/d0mh00396d

rsc.li/materials-horizons

Two-dimensional Dirac spin-gapless semiconductors with tunable perpendicular magnetic anisotropy and a robust quantum anomalous Hall effect†

Qilong Sun, *[a] Yandong Ma[b] and Nicholas Kioussis *[a]

A major recent breakthrough in materials science is the emergence of intrinsic magnetism in two-dimensional (2D) crystals, which opens the door to more cutting-edge fields in the 2D family and could eventually lead to novel data-storage and information devices with further miniaturization. Herein we propose an experimentally feasible 2D material, Fe_2I_2, which is an intrinsic room-temperature ferromagnet exhibiting perpendicular magnetic anisotropy (PMA). Using first-principles calculations, we demonstrate that single-layer (SL) Fe_2I_2 is a spin-gapless semiconductor with a spin-polarized Dirac cone and linear energy dispersion in one spin channel, exhibiting promising dissipation-less transport properties with a Fermi velocity up to 6.39×10^5 m s^{-1}. Our results reveal that both strain and ferroelectric polarization switching could induce an out-of- to in-plane spin reorientation in the 2D Fe_2I_2 layer, revealing its advantage in assembling spintronic devices. In addition, spin–orbit coupling (SOC) triggers a topologically nontrivial band gap of 301 meV with a nonzero Chern number ($|C| = 2$), giving rise to a robust quantum anomalous Hall (QAH) state. The 2D crystal also exhibits high carrier mobilites of 0.452×10^3 and 0.201×10^3 cm^2 V^{-1} s^{-1} for the electrons and holes, respectively. The combination of these unique properties renders the 2D Fe_2I_2 ferromagnet a promising platform for high efficiency multi-functional spintronic applications.

New concepts

The recently discovered 2D magnetic atomic crystals provide unique opportunities for both fundamental studies and technological advances. However, despite extensive efforts, great challenges remain for the practical use of 2D magnets concerning the Curie temperature, non-volatility, and low-power switching. In this manuscript, we demonstrate that the 2D ferromagnetic Fe_2I_2 material exhibits rare perpendicular magnetic anisotropy (PMA) and high Curie temperatures, giving an easier operation scheme and higher stability for the recorded data against thermal fluctuations during reading. In contrast to the insulating magnetic CrI_3 and $Cr_2Ge_2Te_6$ layers, Fe_2I_2 is an intrinsic Dirac half-metal with high carrier mobility and 100% spin polarization, and possesses diverse application prospects for developing nanodevices. Besides, we also reveal that the 2D pristine Fe_2I_2, rather than conventional ferromagnetic thin films, could also be used as 'building blocks' to construct a multiferroic $Fe_2I_2/BaTiO_3$ bilayer towards low-power switching. Finally, spin–orbit coupling (SOC) triggers a topologically nontrivial band gap of 301 meV with a nonzero Chern number ($|C| = 2$), giving rise to a quantum anomalous Hall (QAH) state. Thus, we believe that these intriguing findings will spark much attention in the community of engineers, chemists and physicists working on magnetic nanodevices.

Introduction

The discovery of intrinsic magnetism in van der Waals crystals has attracted tremendous attention in the past few years and has expanded the scope of investigating intriguing phenomena in two-dimensional (2D) materials.[1–4] It is generally known that 2D magnets are prohibited to exhibit long-range magnetic order due to the strong thermal fluctuations revealed by the Mermin–Wagner theorem.[5] However, the recent advances in 2D magnetic van der Waals crystals show that the presence of uniaxial magnetocrystalline anisotropy (MCA) can counteract the thermal agitation and stabilize the long-range magnetism.[1,6,7] Several notable 2D magnets have been observed in magnetic van der Waals (vdW) layers, such as $Cr_2Ge_2Te_6$ and CrI_3, which could retain their magnetism down to the monolayer limit.[1,6,8] In addition, these 2D magnetic crystals also provide flexible 'building blocks' to fabricate versatile vdW heterostructures with new exciting directions. For instance, the antiferromagnetic (AFM) interlayer exchange in bilayer CrI_3 may disclose the full advantage of vdW antiferromagnets for ultrafast, low-power, high-frequency spintronics.[2] Therefore, 2D magnetic systems, combined with their rich electronic and optical properties, constitute ideal platforms to explore new physics in low-dimensional materials as well as numerous opportunities for future device applications.[9,10]

[a] *Department of Physics and Astronomy, California State University, Northridge, California, USA. E-mail: long.q.sun@gmail.com, nick.kioussis@csun.edu*

[b] *School of Physics, State Key Laboratory of Crystal Materials, Shandong University, Jinan, People's Republic of China*

† Electronic supplementary information (ESI) available: Relevant structural, thermal-dynamical, electronic and topological properties for SL Fe_2I_2 (PDF). See DOI: 10.1039/d0mh00396d

A key challenge in searching for and identifying novel 2D magnetic materials is the efficient manipulation of the spin degrees of freedom to give ultra-fast transport and ultra-low energy-consumption.[11] This in turn requires that 2D crystals possess several essential characteristics: room-temperature ferromagnetism,[12] tunable perpendicular magnetic anisotropy (PMA),[13] linear band dispersions for low-energy excitations[14] and half-metallicity.[15–17] Perpendicular magnetic anisotropy (PMA) is essential to give an easier operation scheme and higher stability for the recorded data against thermal fluctuations during reading in devices. However, despite extensive efforts, great challenges remain for the practical use of 2D magnets concerning the Curie temperature, non-volatility, and low-power switching.[17] On the other hand, instead of the flat bands in CrI_3 layers, the graphene-like Dirac bands can eliminate the effective mass of the charge carriers, thus leading to extremely high charge mobility. In addition, half-metals, characterized by one spin channel for conduction around the Fermi level, could provide fully spin-polarized currents and reduce in turn the energy dissipation due to the absence of scattering between different spin channels. Therefore, spin-gapless semiconductors (SGSs) with linear energy dispersions (Dirac SGS) offer a promising platform for spintronic devices.[14,18] In addition, in several two-dimensional Dirac SGS-type materials containing heavy elements, the large spin–orbit coupling (SOC) can trigger a gap opening in one spin channel and drive the system into a quantum anomalous Hall (QAH) state, which is a two-dimensional bulk insulator with a non-zero Chern number in the absence of an external magnetic field. The protected gapless chiral edge states, which are robust against any impurity perturbations, enable dissipationless current transport in spintronic devices. To date the QAH state requires very low temperatures, which restricts its practical applications. Thus, the most critical needs are the material realization of room-temperature and air-stable 2D ferromagnets which exhibit a high Curie temperature, high carrier mobility, and spin-polarized Dirac points close to the Fermi level, and host exotic topological phases. In addition, the electric manipulation of magnetism in 2D Dirac SGS/ferroelectric heterostructures is of great fundamental and technical importance for fast, compact and ultra-low power spintronic devices.[19]

In this work, we identify a compelling 2D material, *i.e.* single layer (SL) Fe_2I_2, with intrinsic ferromagnetism and large spin polarization using first-principles calculations. We demonstrate that the Fe_2I_2 SL with a square lattice is a Dirac SGS with excellent stabilities and moderate mechanical properties. The estimated Curie temperature is considerably higher than room temperature. The conducting spin channel possesses a Fermi velocity up to 6.39×10^5 m s^{-1}, which is superior to most of the reported 2D materials. The revealed perpendicular magnetic anisotropy (PMA) and strain (ferroelectric)-induced spin reorientation render the Fe_2I_2 SL a promising candidate for future spintronics devices. Upon considering SOC, the Dirac cones are deformed with the two chiral edge states, suggesting topologically nontrivial states. Our work shows the enormous potential of the Fe_2I_2 SL in developing 2D magnetism devices.

Computational method

Density functional theory (DFT) calculations were performed in conjunction with the projector augmented wave (PAW) scheme, as implemented in the plane-wave basis Vienna ab initio simulation package (VASP).[20] The generalized gradient approximation (GGA) as formulated by Perdew–Burke–Ernzerhof (PBE) was used for the exchange and correlation functional.[21] A kinetic energy cutoff of 500 eV was employed for the plane-wave expansion of the wave functions and a Monkhorst–Pack scheme of $24 \times 24 \times 1$ k-point sampling was adopted for the integration over the first Brillouin zone.[22] We applied periodic boundary conditions and a vacuum region of 15 Å along the z direction in order to avoid the interactions between two adjacent images. All structures were fully optimized until the residual forces are less than 0.01 eV Å^{-1}. A convergence criterion for the energy of 10^{-6} eV was met. Spin–orbit coupling (SOC) is included in the calculations self-consistently. The DFT+U method was employed for the treatment of the strongly correlated 3d electrons on the Fe orbitals.[23] We adopted $U_{\mathrm{eff}} = 2.5$ eV for the Fe_2I_2 SL, which yields Fe magnetic moments (2.973 μ_B) in excellent agreement with those obtained by the more accurate Heyd–Scuseria–Ernzerhof (HSE06) hybrid functional (3.010 μ_B).[24] The phonon calculation was carried out with a 36-atom $3 \times 3 \times 1$ supercell using the PHONOPY code, which is based on the finite-displacement method.[25] In order to examine the thermal stability, we also performed *ab initio* Born–Oppenheimer molecular dynamics (BOMD) simulations for the same Fe_2I_2 supercell at 300 K and 600 K for 10 ps with a time step of 1 fs.

Results and discussion

Fig. 1(a) shows the fully relaxed geometric structure of the Fe_2I_2 SL, which is similar to the structural prototype of FeOCl.[26] The unit cell contains four atoms, where two co-planar Fe atoms are sandwiched between two layers of I atoms. The 2D Fe_2I_2 SL crystallizes in the orthorhombic $P4/nmm$ space group (no. 129) where the calculated equilibrium lattice constants are $a = b =$ 3.81 Å. Each Fe atom binds to four I atoms with an Fe–I bond length ($l_{\mathrm{Fe-I}}$) of 2.68 Å, which is shorter than that of $\sim$2.83 Å for the layered FeI_2 material.[27] This indicates stronger chemical bonds, hence giving better stability of the Fe_2I_2 SL. To elucidate its bonding characteristics, the electron localization function (ELF) of the selected structural section (highlight in blue lines) is plotted in Fig. S1(a) (see the ESI†). The ELF mainly emerges around the I atoms, while no electronic localization is observed in the area between Fe and I atoms, suggesting ionic bonding between the Fe and I atoms. Besides, the nearest-neighbor Fe–Fe bond length in the middle atomic Fe layer is about 2.69 Å, shorter than that in Fe metal. The metallic bonding of Fe will also contribute to stabilizing the crystal structure.

In order to assess the experimental feasibility and stability of the Fe_2I_2 SL we have calculated the cohesive energy (E_{coh}), the dynamic stability (phonon spectra) and the thermal stability (*ab initio* molecular dynamics simulations). As listed in Table S1 (ESI†)

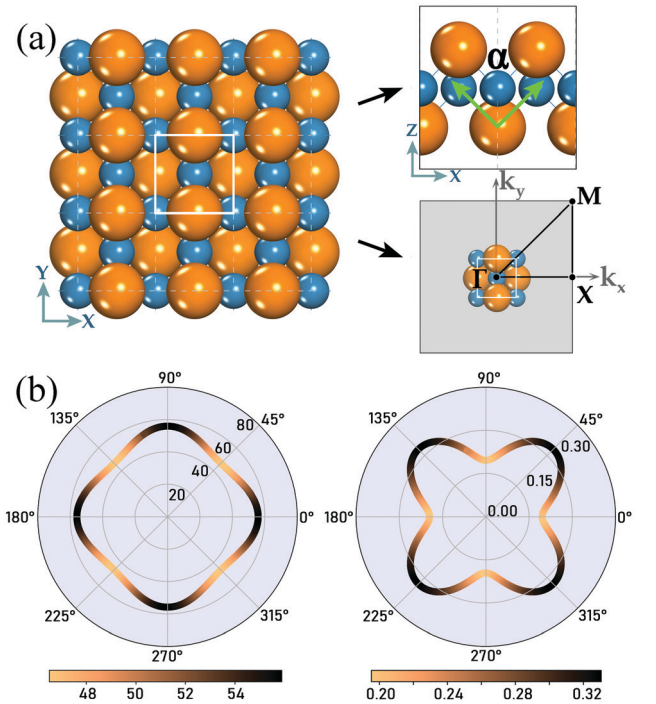

Fig. 1 (a) Top and side views of the Fe_2I_2 SL, where the unit cell is denoted by the white square and the first Brillouin zone is plotted in the right-bottom inset. Blue and orange balls denote the Fe and I atoms, respectively. (b) Angular dependence of the Young's modulus, $Y(\theta)$, and Poisson's ratio, $\upsilon(\theta)$, of the Fe_2I_2 SL, where the angle θ is relative to the x-direction.

the calculated cohesive energy of 3.01 eV per atom (12.03 eV per cell) is comparable to that of the experimentally achieved 2D silicene, phosphorene, and transition metal diiodide layered materials.[28–31] In addition, to confirm its dynamic stability we display in Fig. S1(b) (ESI†) the phonon dispersion curves. One can see that there are no imaginary frequency phonons in the whole Brillouin zone, suggesting a stable minimum of the potential energy surface and hence rendering the monolayer dynamically stable. Besides, the BOMD simulations provide convincing evidence for its thermal stability. More specifically, the 2D pattern can retain its atomic structure up to 500 K for 10 ps (see Fig. S1(c), ESI†), and the corresponding free energy fluctuates slightly during the annealing process, indicating the Fe_2I_2 SL as a promising 2D candidate for various room-temperature applications. Based on the conventional prototypes of the 2D material family, we have constructed seven additional possible configurations of the 2D Fe_xI_y binary materials as shown in Fig. S2 (ESI†). Our results demonstrate that the Fe_2I_2 SL is indeed the ground state crystal structure.

On the other hand, a mechanically stable 2D structure must fulfill the Born–Huang criteria given by C_{11}, C_{22}, $C_{66} > 0$; $C_{11} + C_{22} - 2C_{12} > 0$, where C_{ij} are the elastic constants. In order to further corroborate the mechanical stability of the Fe_2I_2 SL we have calculated the various elastic constants. We find that $C_{11} = C_{22} = 58.11$ N m^{-1}, $C_{12} = 11.35$ N m^{-1}, and $C_{66} = 17.47$ N m^{-1}, complying with the Born–Huang criteria. To elucidate its mechanical performance, the in-plane Young's modulus $Y(\theta)$ and Poisson's ratio $\upsilon(\theta)$ as a function of the angle θ relative to the x direction are shown in Fig. 1(b). The Young's modulus is isotropic along the x and y directions due to the symmetric structure. $Y(\theta)$ changes from 46.50 N m^{-1} to 55.89 N m^{-1} as θ is varied between 0° and 360°. Although the maximum value of $Y(\theta)$ is less than that of graphene (340 N m^{-1})[32] and MoS_2 (128 N m^{-1}),[33] it is still comparable to phosphorene (23–92 N m^{-1})[28,34] and silicene (60 N m^{-1}). The Poisson's ratio $\upsilon(\theta)$ of Fe_2I_2 reaches its largest value of 0.33 along the xy-direction, which is similar to the cases of silicene and MoS_2 layers.[35] These findings demonstrate that the Fe_2I_2 SL has moderate rigidity against deformation and good mechanical properties.

The spin-polarized electronic structure calculations reveal that the ground state of the Fe_2I_2 SL is ferromagnetic, with a magnetic moment of about 3 μ_B per Fe atom (Table S1, ESI†) and an Fe–I–Fe angle ($\angle\alpha$, in Fig. 1(a)) of 90.34°, indicating a ferromagnetic super-exchange interaction according to the Goodenough–Kanamori–Anderson rules.[36] This conjecture was also verified by calculating the exchange energy (E_{exc}), *i.e.* the energy difference between the ferromagnetic (FM) and antiferromagnetic (AFM) phases, $E_{exc} = E_{AFM} - E_{FM}$. As listed in Table S1 (ESI†), E_{exc} is 516 and 478 meV using the GGA+U and HSE06 functional, respectively, indicating that the FM ordering is energetically more favorable. In order to acquire a deeper insight into the stability of the FM state, we have evaluated the temperature dependence of the magnetic moment using Monte Carlo (MC) simulations within the Ising model Hamiltonian, $\hat{H} = -J_{i,j}' \sum_{i,j} \hat{S}_i \hat{S}_j$, for a 100 × 100 2D supercell, where $|\hat{S}| = 3/2$.[37] As shown in Fig. S3 (ESI†), we can see that the magnetic moment is rather insensitive to temperature below 300 K and vanishes at 390 K (GGA+U) and 430 K (HSE06), respectively, turning into paramagnetic states. Therefore, the revealed Curie temperature value (~400 K) is significantly larger than that of the CrI_3 layer (~45 K),[1] the CrOCl SL (~160 K),[3] and $Cr_2Ge_2Te_6$ (~20 K),[6] demonstrating robust ferromagnetism in the Fe_2I_2 SL at room temperature, which is essential for future spintronic applications.

Fig. 2(a) shows the spin-resolved band structure in the absence of SOC. It can be seen that noticeable spin splitting emerges between the two spin channels. The majority-spin is an insulator with an indirect bandgap of 2.37 eV. On the contrary, the valence and conduction energy bands of the minority-spin cross the Fermi level and give rise to two spin-polarized Dirac cones with linear band dispersion, where the Fermi level crosses the spin-polarized Dirac points, along the Γ–X and Γ–Y lines, leading to 100% spin polarization. The three-dimensional (3D) minority-spin band profile around the Fermi level, shown in Fig. 2(b), consists of four Dirac cones in the 2D Brillouin zone (BZ). Note that these Dirac cones in the Fe_2I_2 SL only emerge in the single spin, unlike the case of graphene, revealing the unique feature of SGSs. For SGSs, the massless Dirac fermions with linear dispersion would yield low effective masses and high carrier mobility. In addition, these spin-polarized Dirac points are also well reproduced by the low-energy Hamiltonian $k{\cdot}p$ model in eqn (S1) (ESI†). The calculated Fermi velocities of the electrons and holes are 4.66 × 10^5 m s^{-1} using the GGA+U approach, and 6.39 × 10^5 m s^{-1} for the HSE06 functional,

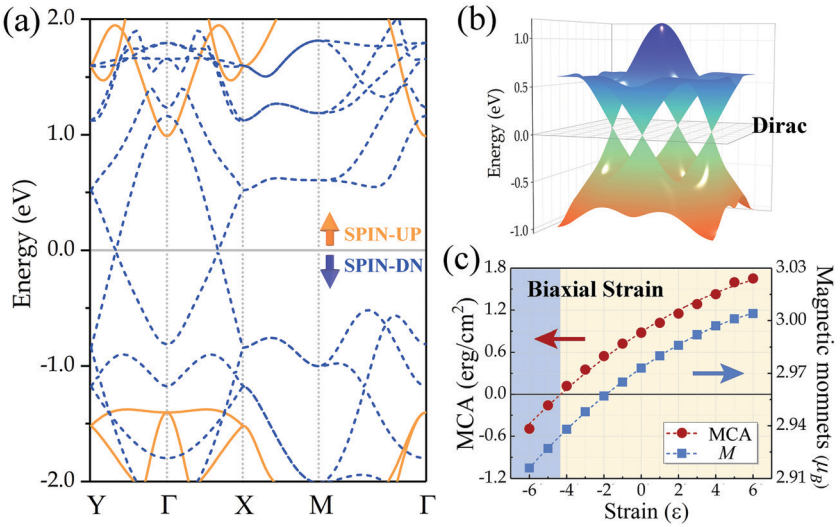

Fig. 2 (a) Spin-resolved band structure of the Fe_2I_2 SL without SOC based on the GGA+U method. (b) 3D band structure close to the Dirac cones. The Fermi level is set at zero. (c) Magnetic anisotropy and magnetic moment per iron atom of the Fe_2I_2 SL as a function of biaxial strain, $\varepsilon(\%) = (a - a_0)/a_0$, where a_0 is the equilibrium lattice constant.

which are comparable with the value of 8×10^5 m s^{-1} in graphene. These outstanding electronic transport properties in one spin channel and the relatively large band gap in the opposite spin channel fulfill the requirement of spin-filtering devices and thus are quite promising for spintronic device applications.

Integration of magnetic 2D materials into promising spintronic devices additionally requires that they exhibit perpendicular magnetic anisotropy (PMA). The magnetocrystalline anisotropy energy (MCA) per unit interfacial area, A, is MCA = $(E_{[100]} - E_{[001]})/A$, where $E_{[100]}$ and $E_{[001]}$ are the total energies with magnetization along the [100] and [001] directions, respectively. The calculated MCA for the Fe_2I_2 SL is 0.80 erg cm^{-2}, indicating an out-of-plane magnetization orientation. This rare PMA in 2D lattices is comparable to those of transition metal thin films,[38] such as FePd, and FoCo films,[39] and higher than the insulating CrI_3 layers.[40] In view of the good mechanical properties, we show the variation of the MCA under external biaxial strain in Fig. 2(c). We find that the PMA increases monotonically with lattice expansion, and reaches a value of 1.65 erg cm^{-2} under a strain of 6%, which is even larger than those of heavy metal capped FeCo junctions,[41] indicating the robustness of the PMA of the 2D Fe_2I_2 system under tensile strain. More interestingly, the system undergoes a spin reorientation transition to an in-plane magnetization orientation beyond −4% compressive strain. To elucidate the underlying mechanism, we also display the variation of the magnetic moment and orbital moment anisotropy ($\Delta M_{orb} = M_{orb}^{[001]} - M_{orb}^{[100]}$) under strain in Fig. 2(c) and Fig. S4 (ESI†), respectively, which correlate well with the corresponding strain variation of the MCA. Similar behaviors have been reported in transition metal films under an electric field, instead of strain.[38,39] In addition, significant changes can be observed to the orbital moments of Fe, where ΔM_{orb} increases from 0.036 to 0.060 μ_B under external strain, consistent with Bruno's expression.[32]

For Dirac states, the presence of SOC usually triggers gap opening at the touching points, leading to intriguing QAHE states. Fig. 3(a) shows the atom- and spin-resolved band structure of the 2D Fe_2I_2 layer with and without SOC. We find that the Fe-d derived states contribute solely to the minority-spin Dirac states near the Fermi level. The I p-derived states mainly lie in the majority spin with the energy range above 1.0 eV and below −1.0 eV *versus* the Fermi level. The d-derived Dirac cones in the 2D Fe_2I_2 layer are different from those

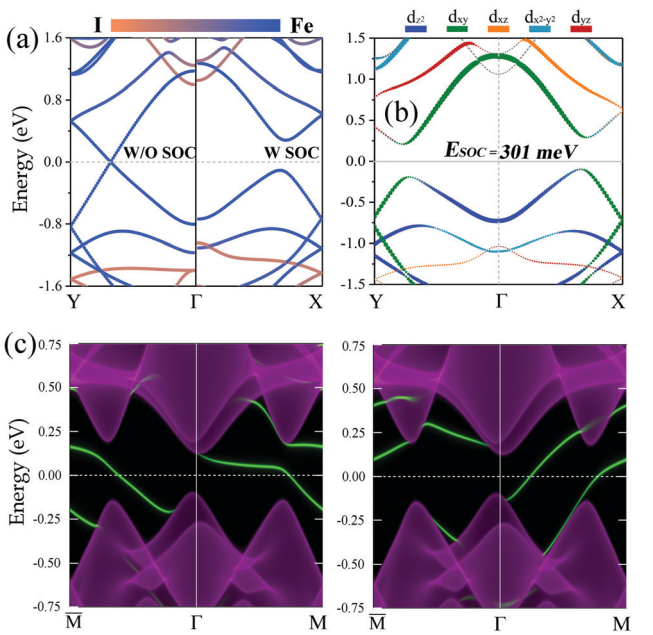

Fig. 3 (a) Energy and k contribution of atom-resolved band structures without (Y–Γ) and with (Γ–X) SOC. (b) The d-orbital character of the minority-spin bands along the symmetry directions for Fe with SOC. The color intensity shows the amplitude of the atom and/or orbital-resolved character. (c) Band structure of the two in-plane edges of the Fe_2I_2 ribbon, with the green edge states connecting the 2D valence and conduction bands.

reported for the 2D MnI_3 layer, which are primarily derived from the I/p states.[9] The bandgap opening of 301 meV in the minority-spin state is induced by the SOC, while the SOC constant is about 54 and 628 meV for Fe and I, respectively. It is noteworthy that another advantage of the Fe_2I_2 SL is that the Fermi level is located exactly inside the SOC-induced bandgap. Therefore, the band-gap effect can be observed directly at room temperature, and there is no need to regulate the chemical potential by gate voltages or doping in experiments.

The degeneracy of the Dirac-like states with SOC will in turn strongly influence the carrier mobilities. Therefore, we have calculated the carrier mobilities along the x and y directions based on the deformation potential theory of Bardeen and Shockley.[42] For a given 2D system, the expression within the phonon-limited scattering model for the mobility of the ith band is $\mu^i = \frac{e\hbar^3 C}{k_B T m^* m_d (E_l^i)^2}$, where T is the temperature, and k_B is the Boltzmann constant; m^*, C, and E_l^i denote the carrier effective mass, elastic modulus, and deformation potential constant, respectively. The average effective mass m_d is obtained by $m_d = \sqrt{m_x^* m_y^*}$, and the x and y directions are indicated in Fig. 1(a). These parameters and the calculated carrier mobilities are presented in Table 1. We find that these quantities show a moderate isotropy characteristic along the x and y transport directions because of the symmetric crystal structure.[43] The calculated room-temperature electron- and hole- mobilities are 0.452×10^3 and 0.201×10^3 $cm^2 V^{-1} s^{-1}$, respectively, which are superior to those of the well-known MoS_2, and comparable with other 2D frameworks.[44]

In order to elucidate the underlying origin of the band structure with SOC we display in Fig. 3(b) the orbital-resolved band structure. We find that the gap states near the Fermi level in the VB (CB) arise mainly from the minority-spin Fe-derived d_{xy} and d_{z^2} ($d_{x^2-y^2}$, d_{yz}, and d_{xy}) orbitals. In view of the band inversion around Γ, we have calculated the Chern number of the Fe_2I_2 SL based on maximally localized Wannier functions to verify the topologically nontrivial states.[45,46] The Chern invariant can be determined by integrating the Berry curvature, $\Omega_z(k)$, of the occupied bands over k-space, $C = \frac{1}{2\pi}\int_{BZ} d^2k \Omega_z(k)$. We find that the Chern number acquires an integer value of 2, suggesting that the Fe_2I_2 SL is a QAH insulator with a topological nontrivial gap. To corroborate this finding, we have also calculated the band structure of the two edges of the semi-infinite Fe_2I_2 ribbon along the x and y directions, respectively, which are displayed in Fig. 3(c). The emergence of two chiral topologically protected gapless edge states circulating around the edges is an important signature of nontrivial 2D TIs, consistent with the calculated Chern invariant. These unique topological properties offer new opportunities for exploring the QAH effect above room temperature.

Having determined the topological nontrivial gap of the 2D Fe_2I_2 SL, next we investigate the influence of external strain on the QAH effect. In Fig. S5 (ESI†) we show the variation of the SOC-induced energy gap of the Fe_2I_2 SL as a function of the in-plane lattice constant (a). We can see that the gap increases linearly with increasing lattice constant a. This linear modulation of the bandgap can facilitate the precise control and observation of the 2D Fe_2I_2 crystal at room-temperature in experiments. In addition, we have calculated the band structure of the edges of the semi-infinite Fe_2I_2 ribbon along the two directions as a function of different in-plane lattice constant (a), and the corresponding results are shown in Fig. S6 (ESI†). We can see that, regardless of the gap value, two chiral topologically protected gapless edge states emerge between the surface states, giving a Chern number of 2. These results clearly demonstrate that 2D Fe_2I_2 crystals possess robust QAH states under biaxial strain.

In contrast to pristine 2D materials, two-phase artificial systems, consisting of FM thin films grown epitaxially on ferroelectric (FE) substrates, would lead to a more intriguing magnetoelectric (ME) effect at room temperature. In contrast to the hexagonal structures reported today, the square crystal lattice of the Fe_2I_2 SL provides a better lattice match with the traditional tetragonal FE or other insulator substrates, contributing to the high-quality epitaxial growth of various magnetic junctions. It is thus of great interest to explore the magnetic anisotropy behaviors with an appropriate ferroelectric substrate, such as the well-known tetragonal $BaTiO_3$ (BTO).[47] To construct the Fe_2I_2/BTO bilayer (see Fig. S7, ESI†), we have considered three different stacking orders for each polarization direction, *i.e.* I atoms atop the O and Ti atoms and hollow site, respectively. Here, the in-plane lattice constant of the Fe_2I_2/BTO bilayer adopted the experimental lattice value of BTO ($\sim$3.992 Å) since the 2D Fe_2I_2 holds good mechanical properties as shown in Fig. 4(a) and Fig. S7 (ESI†). Our results show that the ground state for Fe_2I_2/BTO with the down polarization ($P_\downarrow$) direction corresponds to the stacking configuration where I atoms are atop the hollow site, denoted as $C_G^\downarrow$ (left panel in Fig. 4a). On the other hand, for the up polarization ($P_\uparrow$) direction the ground state corresponds to the atomic configuration where I atoms are atop Ti atoms, denoted as $C_G^\uparrow$ (central panel in Fig. 4b). Here, the distance between the interfacial Ti and I is about 2.91 Å, revealing weak bonding compared with that of Fe–I ($\sim$2.68 Å). Interestingly, we find that for the up-polarization direction there is a metastable configuration (denoted by $C_M^\uparrow$) corresponding to the $C_G{}^\downarrow$ configuration shown in the right panel of Fig. 4(a), whose energy is 181 meV higher than that of $C_G^\uparrow$. One can see that the Fe_2I_2 SL can keep its planar crystal lattice without any distortions after full relaxation, revealing the perfect match with the BTO substrate. Fig. 4(b) shows the variation of the MCA from total energy calculations (black dots) upon polarization switching. We find that the ferroelectric BTO substrate has a dramatic effect on the magnetic properties of the Fe_2I_2 SL, leading to a spin reorientation upon polarization switching. More specifically,

Table 1 Carrier effective masses ($m_{x(y)}/m_0$), deformation potential constant E_l^i(eV), elastic modulus C (J m^{-2}), and carrier mobilities μ ($\times 10^3$ $cm^2 V^{-1} s^{-1}$) for the Fe_2I_2 SL with SOC

Fe_2I_2	m_x	m_y	E_{lx}	E_{ly}	C_x	C_y	μ_x	μ_y
Electron	0.511	0.559	4.791	5.029	58.91	61.67	0.201	0.174
Hole	0.563	0.596	3.060	2.905	58.91	61.67	0.412	0.452

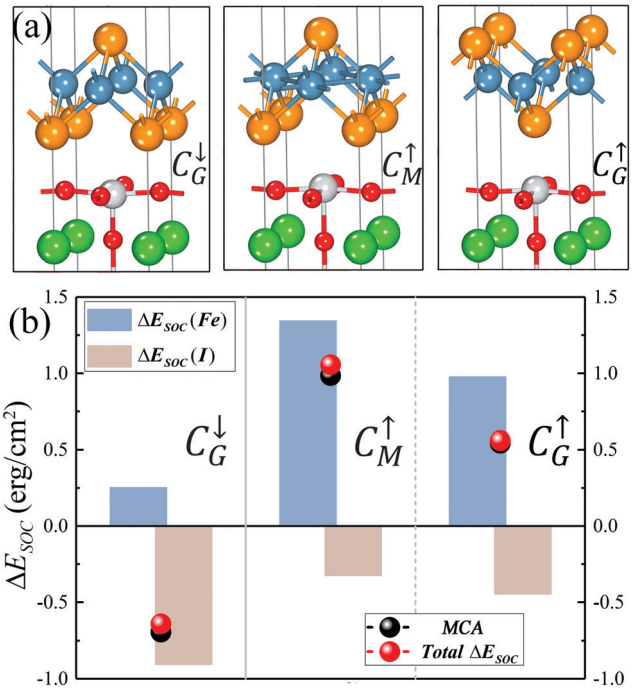

Fig. 4 (a) The ground states of Fe_2I_2/BTO junctions with down ($C_G^{\downarrow}$) and up ($C_G^{\uparrow}$) polarization directions as well as the $C_M^{\uparrow}$ configuration, which could be a metastable state. (b) Total SOC energy differences between the in- and out-of-plane magnetization orientation, ΔE_{SOC} (red dots), and MCA energies (black dots) of the Fe_2I_2/BTO heterostructure with up and down polarization directions. Bar graphs represent the atom-resolved ΔE_{SOC}, for the Fe (light blue) and I (brown) atoms respectively.

the MCA changes from -0.69 erg cm^{-2} (in-plane magnetization orientation) ($C_G{}^{\downarrow}$) to 0.54 erg cm^{-2} ($C_G^{\uparrow}$) (out-of-plane orientation) upon polarization reversal. Note that the MCA of the metastable configuration for the up polarization is also positive with a value of 0.99 erg cm^{-2}, indicating that the polarization reversal is responsible for the spin reorientation. Therefore, the Fe_2I_2/BTO junctions may be promising to be key components in novel data storage and sensing device applications.

In order to understand the underlying mechanism of the spin reorientation behavior *via* ferroelectric polarization switching we have calculated the SOC energy difference (ΔE_{SOC}, see the ESI†) between the in- and out-of-plane magnetization directions, as shown in Fig. 4(b). The calculated ΔE_{SOC} values are -0.64, 1.05, and 0.56 erg cm^{-2} for the three configurations, respectively, which agree well with the MCA values (MCA $\approx$ ΔE_{SOC}). The atom-resolved ΔE_{SOC} shows that Fe solely contribute to the PMA and, on the contrary, I atoms give rise to the in-plane MCA. The polarization reversal does not only enhance the ΔE_{SOC} of Fe from $\sim$0.25 to $\sim$1.0 erg cm^{-2}, but also increases the ΔE_{SOC} of I atoms by 0.5 erg cm^{-2}, resulting in the spin reorientation.

Finally, we have also investigated the robustness of the QAH state of the Fe_2I_2/BTO heterostructures from two aspects, *i.e.* the interfacial ME effect and strain effect. As shown in Fig. S8 (ESI†), we plot the Fe_2I_2 layer-resolved band structure for the three different Fe_2I_2/BTO junctions. Generally, the top layer of Fe_2I_2 maintains its own band dispersion under polarization switching of BTO. Note that the Dirac features in the single spin are also well preserved under the intricate ME effect, strain effect and different stacking order, suggesting a robust Dirac SGS. Here, the ferroelectric polarization switching from $P_{\downarrow}$ to $P_{\uparrow}$ triggers a rigid shift of the Fermi level to a higher chemical potential of the Fe_2I_2/BTO bilayer. This can be mainly attributed to the charge accumulation at the interface for $P_{\uparrow}$. In view of the confirmed nontrivial gap for 2D Fe_2I_2 with an in-plane lattice constant of 3.992 Å as shown in Fig. S6(a) (ESI†), we believe that the Fe_2I_2 top-layer can still provide QAH states under multiple perturbations in the bilayer heterostructure.

Conclusion

In summary, we propose an intriguing 2D SGS, SL Fe_2I_2, which has a ferromagnetic ground state. Unlike most 2D magnetic systems, which possess in-plane magnetocrystalline anisotropy, the Fe_2I_2 SL exhibits intrinsic perpendicular magnetic anisotropy (PMA) and exceedingly strong strain dependence. Many unique properties were unveiled in the Fe_2I_2 SL, including excellent dynamic and thermal stabilities, moderate mechanical performance, a colossal Fermi velocity up to 6.39 $\times$ 10^5 m s^{-1}, and a high Curie temperature $\sim$ 400 K. Intrinsic SOC opens up a global band gap of 301 meV with a Chern number of $|C|$ = 2. The nontrivial topology is further corroborated by the edge states in nanoribbons. We have also demonstrated the emergence of robust QAH states in the 2D Fe_2I_2 crystals under various external perturbations. The estimated electron- and hole-mobilities are up to 0.452 $\times$ 10^3 and 0.201 $\times$ 10^3 cm^2 V^{-1} s^{-1} respectively. In addition, we also demonstrated that the Fe_2I_2 SL undergoes an in-plane to out-of-plane spin reorientation *via* ferroelectric polarization switching. These findings provide opportunities to harvest a robust QAH effect and feasible 2D FM Chern insulators for various spintronic applications and call for experimental investigations.

Conflicts of interest

There are no conflicts to declare.

Acknowledgements

The authors would like to thank Xiaoting Zhou, Cheng-yi Huang, and Xin Lin for useful discussions. The work is supported by NSF-Partnership in Research and Education in Materials (PREM) Grant No. DMR-1828019 and by NSF ERC-Translational Applications of Nanoscale Multiferroic Systems (TANMS) Grant No. 1160504. Q. S. was partially supported by the U.S. Army under Grant No. W911NF-15-1-0066.

References

1 B. Huang, G. Clark, E. Navarro-Moratalla, D. R. Klein, R. Cheng, K. L. Seyler, D. Zhong, E. Schmidgall, M. A. McGuire, D. H. Cobden, W. Yao, D. Xiao, P. Jarillo-Herrero and X. Xu, *Nature*, 2017, **546**, 270–273.

2 M. Gibertini, M. Koperski, A. F. Morpurgo and K. S. Novoselov, *Nat. Nanotechnol.*, 2019, **14**, 408–419.
3 N. Miao, B. Xu, L. Zhu, J. Zhou and Z. Sun, *J. Am. Chem. Soc.*, 2018, **140**, 2417–2420.
4 C. Zhang, Y. Nie, S. Sanvito and A. Du, *Nano Lett.*, 2019, **19**, 1366–1370.
5 N. D. Mermin and H. Wagner, *Phys. Rev. Lett.*, 1966, **17**, 1133.
6 C. Gong, L. Li, Z. Li, H. Ji, A. Stern, Y. Xia, T. Cao, W. Bao, C. Wang, Y. Wang, Z. Q. Qiu, R. J. Cava, S. G. Louie, J. Xia and X. Zhang, *Nature*, 2017, **546**, 265–269.
7 X. Z. Wang, K. Z. Du, Y. Y. F. Liu, P. Hu, J. Zhang, Q. Zhang, M. H. S. Owen, X. Lu, C. K. Gan, P. Sengupta, C. Kloc and Q. H. Xiong, *2D Mater.*, 2016, **3**, 031009.
8 J. Shang, X. Tang, X. Tan, A. Du, T. Liao, S. C. Smith, Y. Gu, C. Li and L. Kou, *ACS Appl. Nano Mater.*, 2020, **3**, 1282–1288.
9 Q. L. Sun and N. Kioussis, *Phys. Rev. B*, 2018, **97**, 094408.
10 S. A. Wolf, D. D. Awschalom, R. A. Buhrman, J. M. Daughton, S. von Molnar, M. L. Roukes, A. Y. Chtchelkanova and D. M. Treger, *Science*, 2001, **294**, 1488–1495.
11 X. T. Wang, T. Z. Li, Z. X. Cheng, X. L. Wang and H. Chen, *Appl. Phys. Rev.*, 2018, **5**, 041103.
12 Q. Sun and N. Kioussis, *Nanoscale*, 2019, **11**, 6101–6107.
13 F. Zheng, J. Zhao, Z. Liu, M. Li, M. Zhou, S. Zhang and P. Zhang, *Nanoscale*, 2018, **10**, 14298–14303.
14 X.-L. Wang, *Natl. Sci. Rev.*, 2017, **4**, 252–257.
15 Y. Jiao, F. Ma, C. Zhang, J. Bell, S. Sanvito and A. Du, *Phys. Rev. Lett.*, 2017, **119**, 016403.
16 C. Zhang, Y. Jiao, L. Kou, T. Liao and A. Du, *J. Mater. Chem. C*, 2018, **6**, 6132–6137.
17 C. Gong and X. Zhang, *Science*, 2019, **363**, eaav4450.
18 X. L. Wang, *Phys. Rev. Lett.*, 2008, **100**, 156404.
19 Q. Sun, S. Kwon, M. Stamenova, S. Sanvito and N. Kioussis, *Phys. Rev. B*, 2020, **101**, 134419.
20 G. Kresse and J. Furthmuller, *Phys. Rev. B: Condens. Matter Mater. Phys.*, 1996, **54**, 11169–11186.
21 J. P. Perdew, K. Burke and M. Ernzerhof, *Phys. Rev. Lett.*, 1996, **77**, 3865–3868.
22 H. J. Monkhorst and J. D. Pack, *Phys. Rev. B: Solid State*, 1976, **13**, 5188–5192.
23 V. I. Anisimov, F. Aryasetiawan and A. I. Lichtenstein, *J. Phys. Condens. Mat.*, 1997, **9**, 767–808.
24 J. Heyd, G. E. Scuseria and M. Ernzerhof, *J. Chem. Phys.*, 2003, **118**, 8207–8215.
25 A. Togo and I. Tanaka, *Scripta Mater.*, 2015, **108**, 1–5.
26 N. Mounet, M. Gibertini, P. Schwaller, D. Campi, A. Merkys, A. Marrazzo, T. Sohier, I. E. Castelli, A. Cepellotti, G. Pizzi and N. Marzari, *Nat. Nanotechnol.*, 2018, **13**, 246–252.
27 M. Ashton, D. Gluhovic, S. B. Sinnott, J. Guo, D. A. Stewart and R. G. Hennig, *Nano Lett.*, 2017, **17**, 5251–5257.
28 Y. Wang, F. Li, Y. Li and Z. Chen, *Nat. Commun.*, 2016, **7**, 11488.
29 B. Feng, Z. Ding, S. Meng, Y. Yao, X. He, P. Cheng, L. Chen and K. Wu, *Nano Lett.*, 2012, **12**, 3507–3511.
30 H. Liu, A. T. Neal, Z. Zhu, Z. Luo, X. Xu, D. Tomanek and P. D. Ye, *ACS Nano*, 2014, **8**, 4033–4041.
31 M. A. McGuire, *Crystals*, 2017, **7**, 121.
32 C. Lee, X. Wei, J. W. Kysar and J. Hone, *Science*, 2008, **321**, 385–388.
33 Y. Cai, G. Zhang and Y. W. Zhang, *J. Am. Chem. Soc.*, 2014, **136**, 6269–6275.
34 L. Wang, A. Kutana, X. Zou and B. I. Yakobson, *Nanoscale*, 2015, **7**, 9746–9751.
35 D. Akinwande, C. J. Brennan, J. S. Bunch, P. Egberts, J. R. Felts, H. Gao, R. Huang, J.-S. Kim, T. Li, Y. Li, K. M. Liechti, N. Lu, H. S. Park, E. J. Reed, P. Wang, B. I. Yakobson, T. Zhang, Y.-W. Zhang, Y. Zhou and Y. Zhu, *Extreme Mech. Lett.*, 2017, **13**, 42–77.
36 J. B. Goodenough, *Interscience*, Wiley, New York, 1963.
37 J. Zhou and Q. Sun, *J. Am. Chem. Soc.*, 2011, **133**, 15113–15119.
38 X. L. Sui, T. Hu, J. F. Wang, B. L. Gu, W. H. Duan and M. S. Miao, *Phys. Rev. B*, 2017, **96**, 041410.
39 P. V. Ong, N. Kioussis, P. K. Amiri, J. G. Alzate, K. L. Wang, G. P. Carman, J. Hu and R. Q. Wu, *Phys. Rev. B: Condens. Matter Mater. Phys.*, 2014, **89**, 094422.
40 W. B. Zhang, Q. Qu, P. Zhua and C. H. Lam, *J. Mater. Chem. C*, 2015, **3**, 12457–12468.
41 P. V. Ong, N. Kioussis, D. Odkhuu, P. K. Amiri, K. L. Wang and G. P. Carman, *Phys. Rev. B: Condens. Matter Mater. Phys.*, 2015, **92**, 020407.
42 J. Bardeen and W. Shockley, *Phys. Rev.*, 1950, **80**, 72–80.
43 J. Qiao, X. Kong, Z. X. Hu, F. Yang and W. Ji, *Nat. Commun.*, 2014, **5**, 4475.
44 B. Radisavljevic, A. Radenovic, J. Brivio, V. Giacometti and A. Kis, *Nat. Nanotechnol.*, 2011, **6**, 147–150.
45 A. A. Mostofi, J. R. Yates, Y.-S. Lee, I. Souza, D. Vanderbilt and N. Marzari, *Comput. Phys. Commun.*, 2008, **178**, 685–699.
46 Q. Wu, S. Zhang, H.-F. Song, M. Troyer and A. A. Soluyanov, *Comput. Phys. Commun.*, 2018, **224**, 405–416.
47 J. P. Velev, C.-G. Duan, J. D. Burton, A. Smogunov, M. K. Niranjan, E. Tosatti, S. S. Jaswal and E. Y. Tsymbal, *Nano Lett.*, 2009, **9**, 427–432.